PROCEEDINGS OF SCIENCE

Modeling Expected TIGERISS Observations

Brian F. Rauch[†,a,*] **and Wolfgang V. Zober**[a] **for the TIGERISS Collaboration**

[a] *Department of Physics and McDonnell Center for the Space Sciences, Washington University, St. Louis, MO 63130 USA*

E-mail: brauch@physics.wustl.edu

The Trans-Iron Galactic Element Recorder for the International Space Station (TIGERISS) is designed to measure the abundances of the rare ultra-heavy Galactic cosmic rays (UHGCRs) $_{30}$Zn and heavier, and is planned to launch to the ISS in 2026. TIGERISS uses planes of crossed silicon strip detectors at the top and bottom for charge (Ohmic side) and trajectory (strip side) determination and acrylic and silica aerogel Cherenkov detectors for velocity and charge determination. Following selection in the second NASA Astrophysics Pioneers Program call, instrument configurations are being studied for available ISS external payload accommodation locations on the Japanese Experiment Module (JEM) "Kibo" Exposed Facility (EF) and the European Space Agency Columbus Laboratory (SOX). Expected UHGCR observations are modelled using differential geometry factors determined for detector orientations within the geomagnetic field over the ISS 51.6° inclination orbit to determine geomagnetic screening. Energy spectra are integrated using the higher of the energy needed to trigger the instrument as a function of incidence angle determined by Geant4 simulations or the energy needed to penetrate the geomagnetic field for time-weighted bins of geomagnetic latitude, instrument orientation, and incidence angle. The expected abundance measurements are reduced by the fraction of events calculated to fragment in the instrument as a function of incidence angle.

38th International Cosmic Ray Conference (ICRC2023)
26 July - 3 August, 2023
Nagoya, Japan

*Speaker

†TIGERISS supported by NASA under cooperative agreement 80NSSC22M0299, the McDonnell Center for the Space Sciences, and the Peggy and Steve Fossett Foundation

PoS(ICRC2023)172

1. Introduction

The Trans-Iron Galactic Element Recorder for the International Space Station (TIGERISS), with a planned launch to the International Space Station (ISS) in 2016, is designed to measure the Galactic cosmic rays (GCRs) from $_5$B to $_{82}$Pb with single-element resolution. It will probe the GCR source (GCRS) and the mechanism that injects material into the GCR accelerator, as well as the sites of rapid neutron capture (r-process) nucleosynthesis. TIGERISS improves upon the preceding TIGER and SuperTIGER balloon-borne instruments by replacing the scintillating fiber hodoscopes for trajectory determination and scintillator detectors for dE/dx measurement with silicon strip detectors (SSDs), which perform both tasks while providing improved charge resolution and linearity, and reduce the material in beam and instrument profile. Event statistics are estimated for TIGERISS based on the method originally derived for and validated with CALET [1, 2] using energy spectra models for the GCRs, accounting for geomagnetic screening in the ISS orbit, detector thresholds, and interaction losses in the instrument.

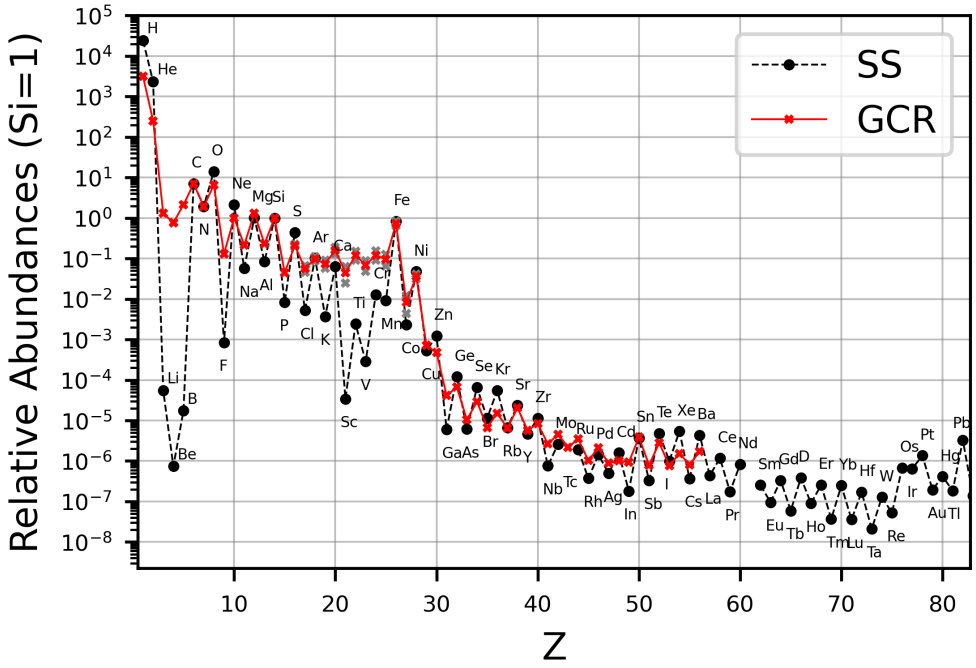

Figure 1: Solar System (SS) [3] and Galactic cosmic-ray (GCR) relative abundances at 2 GeV/nuc. The red line depicts average GCR data, sourced for 1≤Z≤2 from [4], Z=3 from [5], 4≤Z≤28 from [6], and 16≤Z≤56 from [7] normalized to $_{14}$Si. Grey dots depict overlapping measurements from [6] and [7].

Measuring the very rare ultra-heavy Galactic cosmic rays (UHGCRs), $_{30}$Zn and higher charges, with single element resolution is challenging. Figure 1 shows the relative abundances of elements from $_1$H to $_{56}$Ba for GCRs [4–6, 8, 9] with energies of 2 GeV/nucleon compared with the Solar System (SS) abundances [3] through $_{82}$Pb, both normalized to $_{14}$Si = 1. These two samples of interstellar medium (ISM) are broadly consistent, with the much younger few million year old GCRs filling in many of the valleys seen in the ~4.6 billion year old SS, largely from GCR spallation between the GCRS and detection. In the GCRs we see that $_{26}$Fe is ~5×10^3 times less abundant than $_1$H, and that the UHGCRs are ~10^5 times less abundant than $_{26}$Fe. Even-Z elements are typically

more abundant than adjacent odd-Z, being energetically favored with paired proton spins. The SS and UHGCR abundances generally fall with increasing Z, with a notable local increase in the SS around $_{78}$Pt to $_{82}$Pb.

2. TIGERISS Instrument Models

TIGERISS was proposed for the Japan Aerospace Exploration Agency (JAXA) Japanese Experiment Module (JEM) "Kibo" Exposed Facility Unit 10 (JEM-EFU10), but this location is no longer available and we were directed to examine all possible ISS external accommodation locations. We have been developing detailed payload models for attachment to JEM-EFU6 and JEM-EFU7 and the European Space Agency (ESA) Columbus Laboratory external payload Starboard Overhead X-Direction (SOX) location. None of the zenith facing National Aeronautics and Space Administration (NASA) EXpedite the PRocessing of Experiments to the Space Station (ExPRESS) Logistics Carrier (ELC) locations are expected to be available. A technical model of the SOX configuration is shown in Fig. 2a, and it is the new baseline model. Figure 2b shows the JEM-EF standard payload model, and subject to a JAXA waiver, there could be a wider version having a 20 cm greater payload and instrument width. All models include adequate space space for thermal, power and electronics systems below and around the detector stacks.

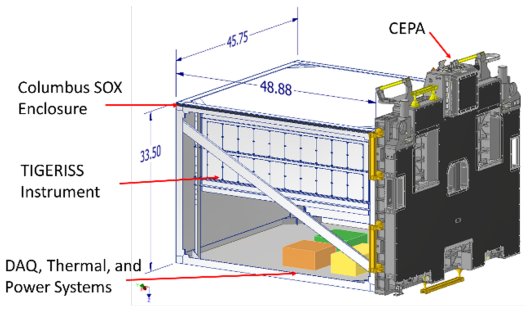

Figure 2(a): Columbus SOX TIGERISS payload technical model.

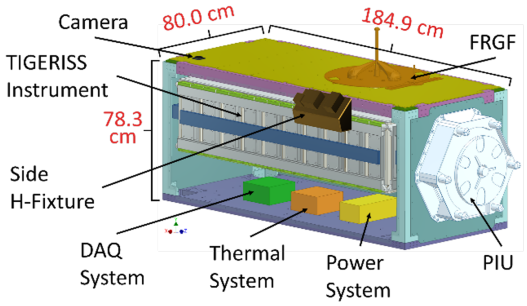

Figure 2(b): JEM-EF standard TIGERISS payload technical model.

Detailed technical models are being developed based on SuperTIGER, in which SSDs replace scintillator detectors and scintillating optical fiber hodoscopes. Orthogonal pairs of SSD arrays at the top and bottom of the instrument measure particle trajectories and ionization energy deposits ($dE/dx \propto Z^2$). Two Cherenkov detectors measure nuclear charge (Z) and velocity (β): C0 with a silica aerogel radiator ($n = 1.05$, $\beta \geq 0.95$, KE $\geq$ 2.12 GeV/nucleon) over C1 with an acrylic radiator ($n = 1.49$, $\beta \geq 0.67$, KE $\geq$ 325 MeV/nucleon).

Geometry factors have been calculated for models of all three ISS accommodation options, with details shown in Table 1. Integral geometry factors from these models are given in Fig. 3a for the Columbus SOX, Fig. 3b for the standard JEM-EF, and Fig. 3c for the wide JEM-EF TIGERISS configurations, showing that most of the acceptance is within ~60°. Despite having the same surface areas, the SOX model has a larger geometry factor than the more elongated standard JEM-EF model.

ISS attachment	length	width	height	area	geometry factor
JEM-EF proposal	1.67 m	0.67 m	0.40 m	1.12 m^2	1.66 m^2 sr
Columbus SOX	1.00 m	0.90 m	0.42 m	0.90 m^2	1.28 m^2 sr
JEM-EF standard	1.50 m	0.60 m	0.42 m	0.90 m^2	1.19 m^2 sr
JEM-EF wide	1.50 m	0.80 m	0.42 m	1.20 m^2	1.83 m^2 sr

Table 1: TIGERISS instrument dimensions and geometry factors.

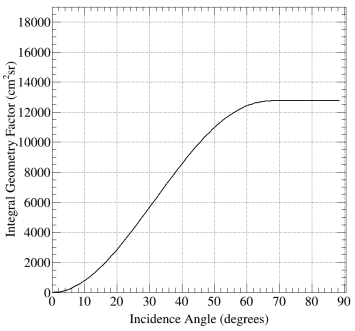

Figure 3(a): ESA Columbus Laboratory external payload configuration: 100.0 cm(L) 90.0 cm(W) 42.0 cm(T) ~1.28 m^2 sr.

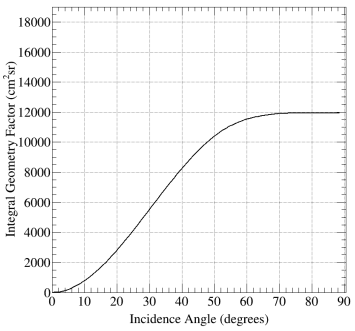

Figure 3(b): JEM-EF standard payload configuration: 150.0 cm(L) 60.0 cm(W) 42.0 cm(T) ~1.19 m^2 sr.

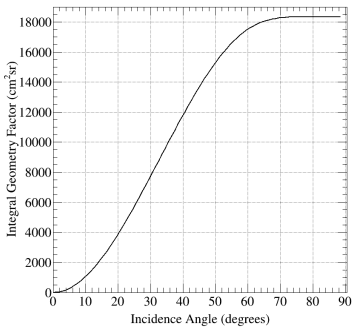

Figure 3(c): JEM-EF rotated payload configuration: 150.0 cm(L) 80.0 cm(W) 42.0 cm(T) ~1.83 m^2 sr.

3. Modelling Geomagnetic Screening

Geomagnetic screening is based on both the strength of the field and the relative orientation of the paths of the charged GCR nuclei to it. GCRs normally incident at the geomagnetic poles travel along the field lines without resistance, while those incident at the equator are most strongly screened. The vertical screening scales with the geomagnetic latitude, and Fig. 4a shows the corresponding vertical cutoff rigidities sampled by the ISS 51.6° orbit at ~400 km, ranging from ~1 to ~15 GV. The screening threshold strength as a function of GCR trajectory, plotted in Fig. 4b relative to the East-West inclination angle (γ) and geomagnetic latitude (λ), is derived from Equation 1, where r is the distance from Earth's center and C_S is the Störmer "constant" derived from the magnetic dipole moment that varies over time with the evolution of Earth's magnetic field:

$$P \geq \frac{1}{r^2} C_S \left(\frac{1 - \sqrt{1 - \cos\gamma \cos^3\lambda}}{\cos\gamma \cos\lambda} \right)^2 . \quad (1)$$

4. East-West Differential Geometry Factors

The instrument acceptance for GCRs isotropically incident at Earth depends on both instrument geometry and the trajectory-dependent geomagnetic screening, where the orientation of the instrument within the geomagnetic field is important. For this analysis we have averaged the expected statistics from cases where the principal axis of the TIGERISS instrument models are aligned with the direction of the geomagnetic field or perpendicular to it. Fig. 5a shows the differential geometry

factor for the SOX model with its major axis aligned with the East-West axis as a function of both the incidence (θ) and East-West (γ) angles, mapped in 1° resolution bins.

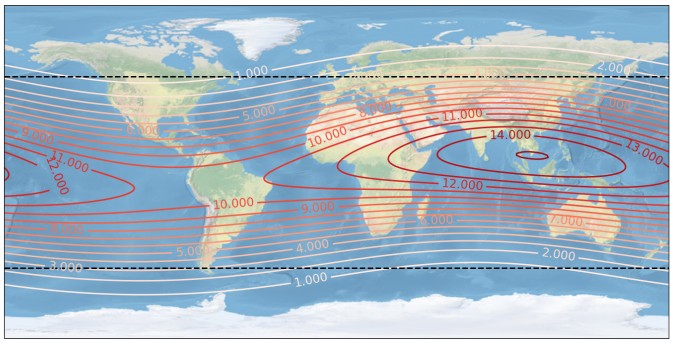

Figure 4(a): Geomagnetic vertical cutoff rigidities sampled by the ISS 51.6° inclination orbit at ~400 km.

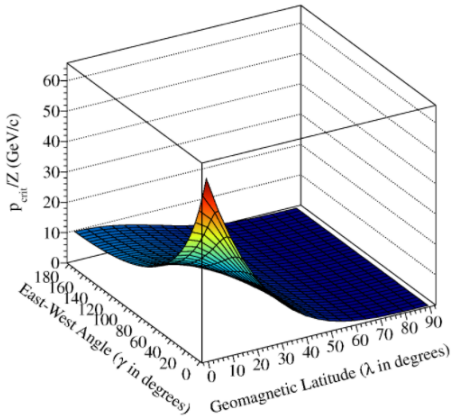

Figure 4(b): Critical momentum to penetrate the geomagnetic field as a function of geomagnetic latitude (λ) and East-West angle (γ).

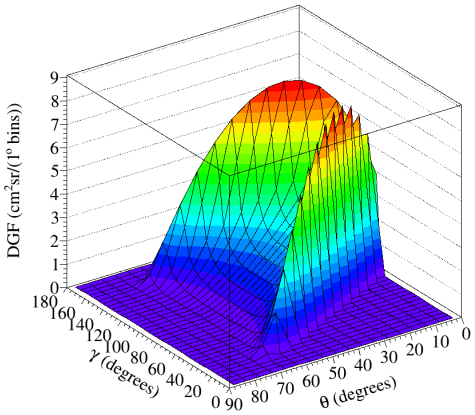

Figure 5(a): TIGERISS SOX instrument differential geometry factor as a function of incidence (θ) and East-West angles (γ) for East-West angle aligned with the instrument major axis.

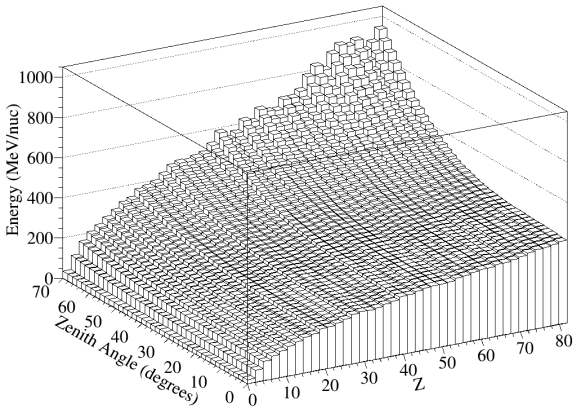

Figure 5(b): Incident threshold energy (MeV/nuc) required to trigger TIGERISS for each element (Z) as a function of incidence angle (θ).

5. Predicting Abundances

The orbital residence times at the different vertical cutoff rigidities shown in Fig. 4a are calculated based on the ISS time at the corresponding geographic latitudes and longitudes to find the weighted vertical cutoff rigidities shown in Fig. 6a. Minimum energy thresholds as a function of East-West angle are derived from the trajectory dependent critical momentum (Eq. 1). The higher of the minimum energy needed to penetrate the geomagnetic field or the incident energy required to trigger the detector determined from Geant4 simulations, shown in Fig. 5b as a function of Z and incidence angle (θ), is used to estimate statistics.

5.1 Estimating GCR Spectra

The energy spectra of elements above $_{28}$Ni have not been measured in the GCRs, so these have to be estimated based on measured or assumed relative abundances. The UHGCRs are mostly primary in composition, so their spectra are derived by scaling the $_{26}$Fe spectrum with relative abundances: HEAO-3-C2 for $Z \leq 26$ [6], TIGER for $26 \leq Z \leq 40$ [8], and HEAO-3-HNE for $Z > 40$ [10]. TIGERISS is expected to see intermediate-to-maximum Solar modulation during its mission, so integral spectra derived from differential spectra in [11] for Solar minimum and maximum are used, as well as averaged spectra.

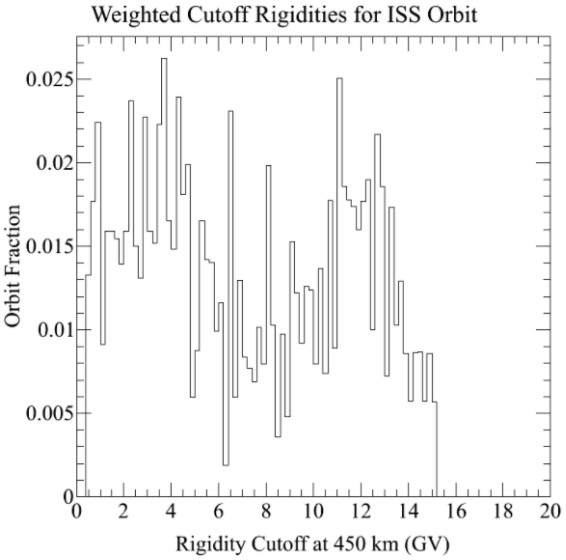

Figure 6(a): The fraction of the ISS orbit spent at each vertical cutoff rigidity.

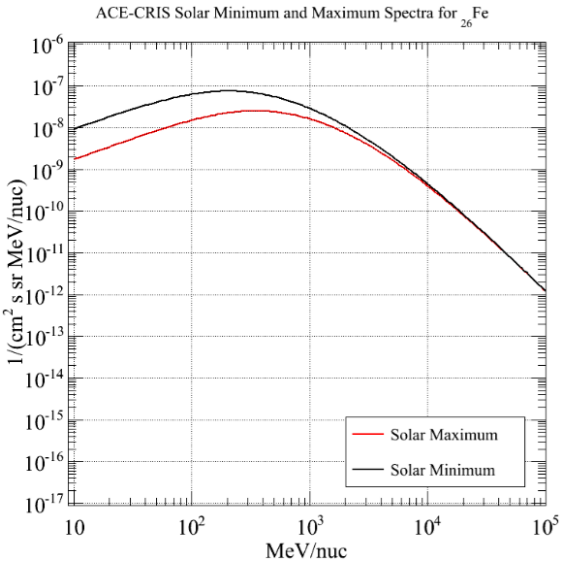

Figure 6(b): Solar maximum and minimum $_{26}$Fe differential energy spectra that are integrated and scaled using relative abundances of heavier elements.

5.2 Estimating Statistics

The abundances that TIGERISS will see for each element are estimated utilizing their integral spectra to find the events expected at each 1° geomagnetic latitude (λ) step as a function of each 1° East-West angle (γ) step. At each γ the integral spectrum of each element is evaluated with the greater of the incident threshold energy (Fig. 5b) or the kinetic energy corresponding to the critical momentum: $E_{crit} = \sqrt{p_{crit}^2/A^2 - m_{amu}} - m_{amu}$, where A is the atomic mass, p_{crit} is the critical momentum, and m_{amu} is the atomic mass unit mass. These fluxes are multiplied by the average of the differential geometry factors with the main instrument axis aligned with the East-West direction (Fig. 5a) and the one with them perpendicular to each other, which are functions of γ and zenith angle, θ. The fluxes for each element are then reduced by the fraction of events calculated to interact in the active area of the instrument and adjusted for the species changing interactions in the inactive material above. The former is done using total charge-changing cross sections given by $\sigma_{tot}(P,T) = \pi[R_P + R_T - (3.20 \pm 0.05)]^2$, where P and T refer to the projectile and target nuclei, and R_P and R_T are their respective nuclear radii [12] for the material areal densities listed in Table 2. The latter correction also uses the partial charge-changing cross sections in [12] to track

the changing element fluxes in the overlying 0.083 g/cm^2 of polystyrene (C_8H_8) and 0.686 g/cm^2 of aluminum. Finally, the numbers of each element expected are found by multiplying the fluxes adjusted for interactions by the total observation time of one year and the geomagnetic latitude orbit fraction shown in Fig. 6a.

detector material	chemical formula	thickness (cm)	density (g/cm^3)	areal density (g/cm^2)
aluminum	Al	0.168	2.700	0.454
silicon	Si	0.400	2.329	0.932
PET	$C_{10}H_8O_4$	0.090	1.135	0.102
PMI	$C_8H_{11}O_2N$	8.732	0.032	0.279
PMMA	$C_5H_8O_2$	1.270	1.180	1.499
Kapton	$C_{22}H_{10}N_2O_5$	0.0127	1.420	0.0180
silica	SiO_2	2.000	0.205	0.410
PE	C_2H_4	0.006	0.919	0.00552
PU	$C_{25}H_{42}N_2O_6$	0.635	0.080	0.0508
PTFE	C_2F_4	0.100	0.600	0.060

Table 2: TIGERISS instrument model materials: polystyrene (PS), aluminum (Al), silicon (Si), polyethylene terephthalate (PET) - Mylar, polymethacrylimide (PMI), polymethyl methacrylate (PMMA) - acrylic, Kapton (polyimide film), polyethylene (PE), polyurethane (PU), polytetrafluoroethylene (PTFE).

6. Results and Discussion

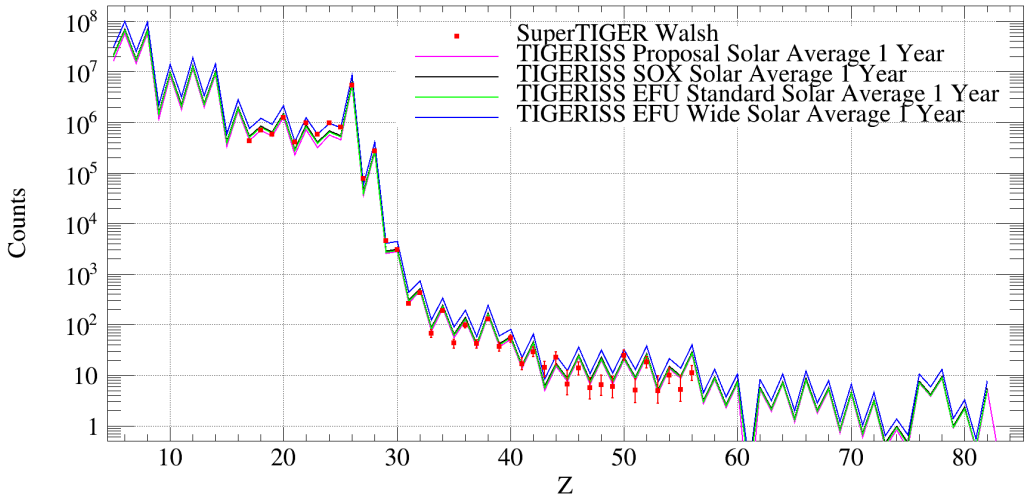

Figure 7: Predicted abundances measured by TIGERISS after 1 year of operation compared to those measured by SuperTIGER over its 55 day long-duration-balloon flight [7, 13].

Elemental abundances predicted for the TIGERISS instrument models after one year of operation on the ISS at average Solar activity are compared to those measured by SuperTIGER during

its 55 day long-duration-balloon flight [7, 13] in Fig. 7. The expected TIGERISS statistics are not strongly dependent on the level of Solar modulation because the geomagnetic screening in the ISS orbit limits the lower-energy nuclei most strongly affected by modulation. The one-year TIGERISS results for all models are comparable to those of SuperTIGER and would be free of the systematic effects from corrections needed to account for atmospheric nuclear interactions and energy losses. The UHGCR statistics from one year would be about half of what HEAO-3-HNE observed, but with single-element resolution through $_{82}$Pb they will have significant exploratory value.

The SOX (black), JEM-EF standard (green) and JEM-EF wide (blue) predictions are slightly better than those from the proposal's JEM-EF model (pink), despite the first two models both having smaller geometry factors. This is due to the use of the improved Z and θ dependent trigger threshold over the fixed one (350 MeV/nuc) used previously. Future improvements will include an updated material list as it is more fully specified during model development, which will likely reduce the material in beam further. Finally, we will implement differential geometry factors for each orientation of the detector models with respect to the East-West angle weighted appropriately for orbit fractions.

7. References

[1] B. F. Rauch for the CALET Collaboration, "Predicted CALET measurements of ultra-heavy cosmic ray relative abundances," *Advances in Space Research*, vol. 53, pp. 1444–1450, May 2014.

[2] B. F. Rauch and Y. Akaike, "Status of the CALET Ultra Heavy Cosmic Ray Analysis," in *Proceedings of 35th International Cosmic Ray Conference — PoS(ICRC2017)*, vol. 301, p. 180, 2017.

[3] K. Lodders, "Solar System Abundances and Condensation Temperatures of the Elements," *The Astrophysical Journal*, vol. 519, pp. 1220–1247, 2003.

[4] T. Sanuki *et al.*, "Precise Measurement of Cosmic-Ray Proton and Helium Spectra with the BESS Spectrometer," *The Astrophysical Journal*, vol. 545, no. 2, pp. 1135–1142, 2000.

[5] M. Aguilar *et al.*, "Isotopic Composition of Light Nuclei in Cosmic Rays: Results from AMS-01," *The Astrophysical Journal*, vol. 736, p. 105, Aug. 2011.

[6] J. J. Engelmann *et al.*, "Charge Composition and Energy Spectra of Cosmic-Ray Nuclei for Elements from Be to Ni. Results from HEAO-3-C2," *Astronomy & Astrophysics*, vol. 233, pp. 96–111, 1990.

[7] N. E. Walsh, *SuperTIGER Elemental Abundances for the Charge Range* $41 \leq Z \leq 56$. PhD thesis, Washington University in St. Louis, 2020.

[8] B. F. Rauch *et al.*, "Cosmic Ray Origin in OB Associations and Preferential Acceleration of Refractory Elements: Evidence from Abundances of Elements $_{26}$Fe through $_{34}$Se," *The Astrophysical Journal*, vol. 697, no. 2, pp. 2083–2088, 2009.

[9] N. E. Walsh *et al.*, "SuperTIGER instrument abundances of galactic cosmic rays for the charge interval $41 \leqslant Z \leqslant 56$," *Advances in Space Research*, vol. 70, pp. 2666–2673, Nov. 2022.

[10] W. R. Binns *et al.*, "Abundances of Ultraheavy Elements in the Cosmic Radiation: Results from HEAO 3," *The Astrophysical Journal*, vol. 346, pp. 997–1009, 1989.

[11] J. S. George *et al.*, "Elemental Composition and Energy Spectra of Galactic Cosmic Rays During Solar Cycle 23," *The Astrophysical Journal*, vol. 698, no. 2, 2009.

[12] B. S. Nilsen *et al.*, "Fragmentation Cross Sections of Relativistic $^{84}_{36}$Kr and $^{109}_{47}$Ag Nuclei in Targets From Hydrogen to Lead," *Physical Review C*, vol. 52, no. 6, pp. 3277–3290, 1995.

[13] N. E. Walsh *et al.*, "SuperTIGER Abundances of Galactic Cosmic Rays for the Atomic Number (Z) Interval 30 to 56," in *Proceedings of 37th International Cosmic Ray Conference — PoS(ICRC2021)*, vol. 395, p. 118, 2021.

Full Author List: TIGERISS Collaboration

R. F. Borda[1], R. G. Bose[2], D. L. Braun[2], J. H. Buckley[2], J. Calderon[3], N. W. Cannady[1,4,5], R. M. Caputo[4], S. Coutu[6], G. A. de Nolfo[7], P. Ghosh[8,4,5], S. Jones[3], C. A. Kierans[4], J. F. Krizmanic[4], W. Labrador[2], L. Lisalda[2], J. V. Martins[1], M. P. McPherson[9], E. Meyer[1], J. G. Mitchell[7], J. W. Mitchell[4], S. I. Mognet[6], A. Moiseev[10,4,5], S. Nutter[3], N. E. Osborn[2], I. M. Pastrana[2], B. F. Rauch[2], H. Salmani[9], M. Sasaki[10,4,5], G. E. Simburger[2], S. Smith[9], H. A. Tolentino[9], D. Washington[6], W. V. Zober[2]

[1]University of Maryland, Baltimore County, [2]Department of Physics and McDonnell Center for the Space Sciences, Washington University in St. Louis, [3]Northern Kentucky University, [4]NASA Goddard Space Flight Center, Astrophysics Science Division, [5]Center for Research and Exploration in Space Sciences and Technology II, [6]Pennsylvania State University, [7]NASA Goddard Space Flight Center, Heliophysics Science Division, [8]Catholic University of America, [9]Howard University, [10]University of Maryland, College Park

PoS(ICRC2023)172